Editors' Suggestion

# Interfacial modulation of spin pumping in YIG/Pt

Lin Liu,[1,*] Yuehui Li,[1,2,*] Yahui Liu,[1] Tao Feng,[3] Jun Xu,[2] X. R. Wang,[4] D. Wu,[3] Peng Gao,[1,2,†] and J. Li[1,‡]

[1]*International Center for Quantum Materials, School of Physics, Peking University, Beijing 100871, China*

[2]*Electron Microscopy Laboratory, School of Physics, Peking University, Beijing 100871, China*

[3]*National Laboratory of Solid State Microstructures, Department of Physics and Collaborative Innovation Center of Advanced Microstructures, Nanjing University, 22 Hankou Road, Nanjing 210093, China*

[4]*Physics Department, The Hong Kong University of Science and Technology, Clear Water Bay, Kowloon, Hong Kong*

(Received 9 April 2020; revised 18 June 2020; accepted 19 June 2020; published 8 July 2020)

Spin transfer across the interface of magnetic insulator/heavy metal is dominated by the magnetic state at interface. Utilizing aberration corrected scanning transmission electron microscopy and electron energy loss spectroscopy, we demonstrate the existence of metallic $Fe^0$ atoms at YIG/Pt interface. The observed spin pumping signal is linearly proportional to total $Fe^0$ magnetic moments at YIG/Pt interface, revealing the critical role of the interfacial magnetic moments on spin transfer. In addition, PtFe alloying might contribute to a channel of spin sink at YIG/Pt interface.

DOI: 10.1103/PhysRevB.102.014411

Interfaces of magnetic structure play a fundamental role in spin-based technologies [1]. By creating the interface between ferromagnetic (FM) thin films and nonmagnetic metal (NM) thin films with strong spin-orbit coupling, the rich physics are involved in FM/NM bilayers and abundant spin-current-related phenomena have been reported. Yttrium iron garnet $Y_3Fe_5O_{12}$ (YIG) thin films are the most prominent candidates for spintronics, magnonics, and spin-caloritronics due to their exceptionally low magnetization damping [2,3]. Magnetic excitations in YIG layers can inject pure spin current into the adjacent NM layers through spin pumping [4] or spin Seebeck effect [5], and spin-orbit coupling in NM layers converts pure spin current to the transverse charge current. Charge current can also be converted to spin current by spin-orbit coupling in NM layers and exerts spin torque on adjacent YIG, inducing spin-orbit torque [6] and spin Hall magnetoresistance (SMR) [7]. All these spin-current-related phenomena require a high efficiency of transferring spin angular momentum across YIG/NM interface, i.e., a high spin mixing conductance [8]. According to local moment model [9], spin mixing conductance is dominated by local magnetic moments at YIG/NM interface where spin transfer acts locally on magnetic ions. Therefore, insertion of a thin FM metallic layer at the YIG/NM interface is expected to enhance significantly the spin mixing conductance. However, experimental studies have shown the contradictory results that the existence of metallic thin FM could significantly reduce spin pumping [10] or enhance spin pumping [11]. It is important to point out that such a puzzling situation is mainly due to a lack of characterization of the magnetic state at the YIG/NM interface, which may obstruct the road to a higher spin mixing conductance and a better performance of spintronics devices. Different YIG/NM interfaces due to different fabrication conditions could easily result in different chemical profiles and magnetism at the interface (e.g., interfacial alloying, contaminations at interface or interfacial chemical reconstruction) [12–15], leading to contradictory experimental results [16]. Therefore, a local and direct probe of YIG/NM interfacial properties (e.g., structural, electronic, and magnetic profiles) is crucial to the understanding of spin-current-related phenomena at the YIG/NM interface.

In this work, we present an atomic-scale investigation of YIG/Pt interface by aberration corrected scanning transmission electron microscopy (STEM) and electron energy loss spectroscopy (EELS). A structurally sharp YIG/Pt interface was confirmed. The existence of metallic $Fe^0$ atoms at YIG/Pt interface was revealed unambiguously. Tailoring YIG/Pt interface by postannealing, the linear dependence of spin pumping signals and total $Fe^0$ magnetic moments was demonstrated, revealing the critical role of the interfacial magnetic moments on spin mixing conductance. Furthermore, spin pumping signal was found to return to zero prior to total $Fe^0$ magnetic moments, indicating a channel of spin sink at YIG/Pt interface. Such spin sink effect may be attributed to the curtailed spin diffusion length in PtFe.

Figure 1(a) shows a low magnification STEM image of gadolinium gallium garnet (GGG)/YIG/Pt sample along the [112] direction. The atomically resolved STEM-high-angle annular dark-field imaging (HAADF) image in Fig. 1(b) shows an atomic sharp interface between YIG and Pt. Figures 1(c) and 1(d) reveal a high-quality single-crystalline YIG film grown epitaxially on GGG substrate [17]. From the $Z$ contrast ($Z$ refers to atomic number) of STEM-HAADF image, the bright atoms are identified to be Y and Fe atom columns. In addition, polycrystalline Pt film (7 nm) grown on GGG/YIG was confirmed. In order to gain a deep insight into the chemical environment of Fe ions in YIG films, Fe $L$-edge spectra were measured by EELS at different locations as the following: "1" spot on Pt side at YIG/Pt interface; "2" spot

*These authors contributed equally to this work.
†Corresponding author: p-gao@pku.edu.cn
‡Corresponding author: jiali83@pku.edu.cn

 

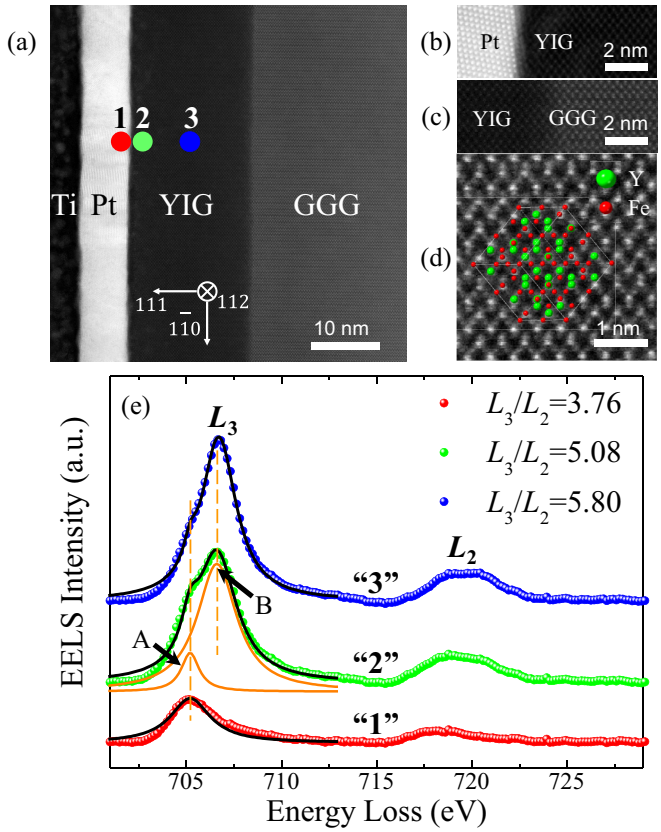


FIG. 1. (a) Low magnification STEM image of GGG/YIG/Pt sample along [112] direction. Atomically resolved STEM-HAADF image of (b) YIG/Pt atomic sharp interface, (c) GGG/YIG interface and (d) high-quality single-crystalline YIG film with labeled atom planes. (e) Fe $L$-edge spectra measured by EELS at three different locations labeled in (a). Fe $L_3$-edge spectra were fitted by the combination of two Lorentzian curves [orange curves in (e)], marked as peak A at 705.2 eV and peak B at 706.6 eV. The black curves (sum of peak A and peak B) in (e) show the best fitting of Fe $L_3$-edge spectra.

on YIG side at YIG/Pt interface and "3" spot in bulk YIG. In Fig. 1(e), Fe $L_3$-edge recorded at spot "1" exhibits the metallic $Fe^0$ nature (an asymmetrical peak A), indicating the diffusion of $Fe^0$ atoms into Pt layer. Fe $L_3$-edge recorded at spot "3" shows the $Fe^{3+}$ feature of a major contribution from peak B and a minor contribution from peak A. If $Fe^{3+}$ valence was mixed by $Fe^{2+}$, the intensity of peak A ($I_A$) would increase with respect to the intensity of peak B ($I_B$). We calculated the intensity ratio of Fe $L_3$ and $L_2$ white lines ($L_3/L_2$ ratio) from these Fe $L$-edge spectra measured by EELS. The $L_3/L_2$ ratio is 5.8 in bulk YIG (spot "3"), corresponding to $Fe^{3+}$ valence state (all Fe atoms should be $Fe^{3+}$ cations in YIG) [3,18]. The $L_3/L_2$ ratio is 3.76 in the interfacial Pt layer (spot "1"), confirming the existence of $Fe^0$ in Pt layer ($L_3/L_2$ ratio is $\sim$ 3.8 for pure Fe metal) [18]. This is direct evidence of $Fe^0$ diffusion into Pt layer, which is also supported by oxygen $K$-edge spectra. The oxygen prepeak and main peak at the $K$ edge are absent in the interfacial Pt layer, which can help to exclude the possible artifacts in EELS measurements of the Fe $L$ edge (see Supplemental Material Fig. S4(g) [19]). The $L_3/L_2$ ratio is 5.08 on the YIG side at YIG/Pt interface (spot "2"), which is in between the values found for $Fe^{2+}$ and $Fe^{3+}$ (the $L_3/L_2$ ratio is $\sim$4.6 for $Fe^{2+}$ and 5.8 for $Fe^{3+}$) [18]. The presence of $Fe^{2+}$ states at YIG/Pt interface has been reported in the literature [20,21], and the correlation between the formation of $Fe^{2+}$ cations and oxygen deficiency was suggested, which might be attributed to the deposition of Pt on YIG. Fe $L_3$-edge spectra recorded at spot "1", "2", and "3" manifest that the distribution of element Fe is broad even YIG/Pt interface is atomic sharp, and $Fe^0$ diffusion into Pt layer is confirmed.

The $L_3/L_2$ ratio is related to the number of holes on Fe d bands at Fermi level, thus behaves similarly to magnetic moment per Fe atom [18]. Changing Fe valence from $Fe^{3+}$ ($3d^5$) to $Fe^{2+}$ ($3d^6$) reduces the number of holes on Fe $d$ bands, resulting in a reduced magnetic moment per Fe atom (from $\sim$5 to $\sim$4 $\mu_B$), which can be characterized by a reduced $L_3/L_2$ ratio from 5.8 to 4.6 [9,22]. Further reducing the number of holes on Fe $d$ bands yields $Fe^0$ and a further reduced magnetic moment per Fe atom (2.2 $\mu_B$), corresponding to $L_3/L_2$ ratio $\sim$3.8. Such monotonic (not linear) dependence of magnetic moment per Fe atom and $L_3/L_2$ ratio encourage us to qualitatively characterize Fe magnetic moment by $L_3/L_2$ ratio [23].

To reveal the evolution of Fe valence state throughout the GGG/YIG/Pt sample, Fe $L$-edge spectra were recorded by EELS line scan with 0.25 nm for each step (see Supplemental Material Fig. S4(b) [19]). $L_3/L_2$ ratios at different locations of sample were calculated based on these Fe $L$-edge spectra. As shown in Fig. 2(b), YIG layer and YIG/Pt interface can be divided into three regions, according to the profile of the calculated $L_3/L_2$ ratios. Region I presents $Fe^{3+}$ valence state in bulk YIG. As described in the previous paragraph, region II contains the mixed valence state of $Fe^{2+}$ and $Fe^{3+}$. A steep decline in $L_3/L_2$ ratios was observed at YIG/Pt interface (from region II to region III), indicating a sharp interface between oxidized Fe and metallic $Fe^0$. Such a sharp interface can also be confirmed by a steep decline of oxygen $K$-edge prepeak at the YIG/Pt interface (Supplemental Material Fig. S4(g) [19]). Therefore, a structurally sharp interface between YIG and Pt was demonstrated unambiguously. Region III was marked by a gradient shadow in Fig. 2(b). $L_3/L_2$ ratios are $\sim$3.8 close to the YIG/Pt interface, thus magnetic moment per $Fe^0$ atom is expected to be $\sim$2.2 $\mu_B$ adjacent to YIG/Pt interface in region III. To simplify the following discussion, such a fraction adjacent to YIG/Pt interface is called the $Fe^0$ enrichment zone ($\sim$1-nm thick). On the contrary, $L_3/L_2$ ratios decrease drastically in region III away from YIG/Pt interface, indicating the drastic reduction of $Fe^0$ magnetic moments deep inside the Pt layer (1.5 nm away from YIG/Pt interface) that is called the $Fe^0$ depletion zone. The drastic reduction of $L_3/L_2$ ratios in the $Fe^0$ depletion zone arises from the reduction of Fe $d$-band holes, which results from the electron transfer between Fe and Pt, indicating PtFe alloying in region III. This electron transfer indicates an effectual hybridization between Fe 3d bands and Pt 5d bands [24], leading to a possible magnetic proximity effect (MPE) at YIG/Pt interface [25]. Such a MPE will be discussed in the Supplemental Material S7 [19].

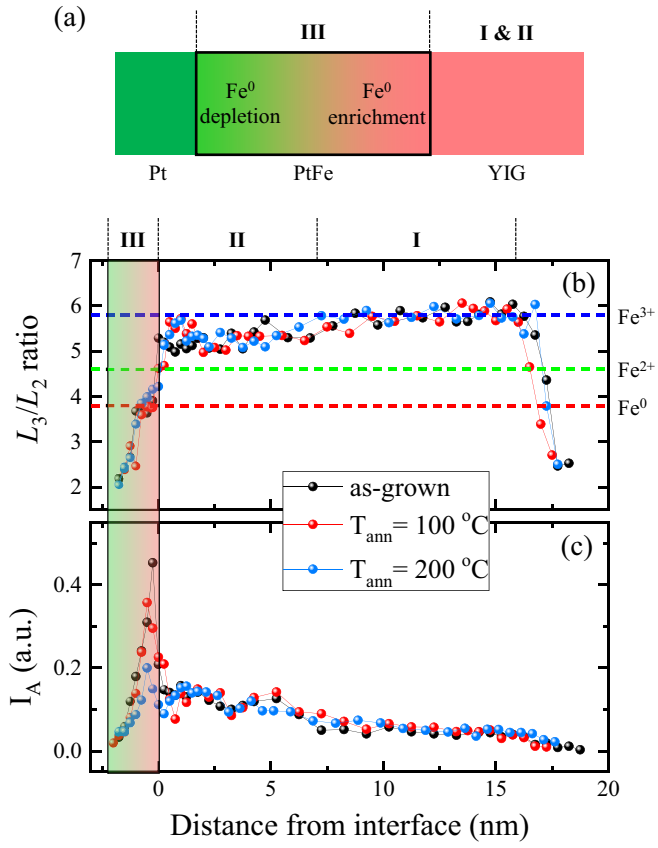


FIG. 2. Chemical profiles of YIG/Pt interface. (a) Illustration of composition profile at YIG/Pt interface. (b) The profiles of $L_3/L_2$ ratios and (c) the normalized peak A intensities ($I_A$) throughout the GGG/YIG/Pt sample, for as-grown sample, sample after postannealing at 100 °C ($T_{\text{ann}} = 100\,^{\circ}\text{C}$), sample after postannealing at 200 °C ($T_{\text{ann}} = 200\,^{\circ}\text{C}$). $I_A$ in region III is entirely assigned to the contributions of $Fe^0$ in Pt layer. The horizontal dashed lines (red, green, and blue) in (b) label the typical $L_3/L_2$ ratios of $Fe^0$, $Fe^{2+}$, and $Fe^{3+}$.

In order to tailor the YIG/Pt interface, the same GGG/YIG/Pt sample was treated by postannealing at different temperatures in sequence (Supplemental Material S1 [19]). The profiles of $L_3/L_2$ ratios obtained after postannealing at 100 °C ($T_{\text{ann}} = 100\,^{\circ}\text{C}$) and 200 °C ($T_{\text{ann}} = 200\,^{\circ}\text{C}$) reproduce the profile of $L_3/L_2$ ratios of the as-grown sample [Fig. 2(b)], supporting the chemical stability of GGG/YIG/Pt sample. The STEM images of the same GGG/YIG/Pt sample after postannealing present the similar ordered lattice of YIG film, demonstrating that the high crystallinity of YIG film can be preserved after postannealing up to 200 °C (see Supplemental Material Figs. S3(a) to 3(c) [19]).

To achieve the quantitative analysis of $Fe^0$ atom density, Fe $L_3$-edge spectra were fitted by the combination of two Lorentzian curves [orange curves in Fig. 1(e), marked as peak A and peak B]. The intensity profiles of $I_A$ were plotted in Fig. 2(c) throughout the GGG/YIG/Pt sample (as-grown, $T_{\text{ann}} = 100\,^{\circ}\text{C}$ and $T_{\text{ann}} = 200\,^{\circ}\text{C}$). $I_A$ in Fig. 2(c) were normalized by the average of $I_{A+B}$ in region I ($I_{A+B} = I_A + I_B$ represents the total intensity of Fe $L_3$-edge, details described in Supplemental Material S4 [19]) [26]. $I_A$ was higher in region II than that in region I, originating from the mixed valence state of $Fe^{2+}$ and $Fe^{3+}$ in region II. In light of the sharp interface between oxidized Fe and metallic $Fe^0$, $I_A$ in region III is entirely assigned to the contributions of $Fe^0$ in Pt layer. Intense $I_A$ and a maximum of $I_A$ were observed in $Fe^0$ enrichment zone from as-grown sample. This $I_A$ maximum of 0.453 represents the local $Fe^0$ atom density with respect to $Fe^{3+}$ ion density in region I. Recalling that $Fe^{3+}$ ion density of bulk YIG is $\sim$10.55 atoms/nm$^3$ in region I [17], $Fe^0$ atom density was estimated to be $\sim$4.78 atoms/nm$^3$ at this maximum location. After postannealing at 100 °C, the $I_A$ profile slightly decreased in region III, the maximum of $I_A$ was 0.357. The $I_A$ profile dramatically decreased in region III after postannealing at 200 °C, the maximum of $I_A$ was reduced to 0.199. Such a dramatic reduction of $I_A$ in region III corresponds to a dramatic reduction of $Fe^0$ atom density inside Pt layer. It is worth mentioning that $I_A$ profiles remain unchanged in regions I and II after postannealing, demonstrating the stability of sample's chemical composition against postannealing. These aforementioned results shown in Fig. 2 are well reproducible (see Supplemental Material S1 [19]), and postannealing is an efficient method to tailor YIG/Pt interface.

Spin pumping in the GGG/YIG/Pt sample was studied via the measurements of voltage signals $V(H)$ along Pt electrodes by sweeping in-plane magnetic field (H). Figure 3(b) shows a representative trace of V(H) data when the azimuthal angle of H($\theta_{\text{H}}$) is 14°. The line shape of V(H) in Fig. 3(b) seems to be symmetric Lorentzian curve. However, spin pumping signals of YIG/Pt samples are reported to be contaminated by the spin rectification effect (SRE) [27], just like SMR, and anomalous Hall effect [28,29]. For the purpose of extracting spin pumping signals ($V_{SP}$) from V(H) data, we carried out angular dependent measurements of V(H) data following the conventional method in the literature [30,31]. The fitting of angular dependent V(H) data confirmed that spin pumping dominated V(H) signals in our measurements (details described in Supplemental Material S6 [19]). SRE is not sufficient to contaminate spin pumping signals, and angular dependent $V_{\text{sym}}$ is approximate to $V_{SP}$. As shown in Fig. 3(d), angular dependent $V_{\text{sym}}$ slightly decreased after postannealing at 100 °C and decreased by one order of magnitude after postannealing at 200 °C, indicating a dramatic reduction of spin pumping across the YIG/Pt interface.

Considering region III as a dusting layer between YIG and Pt, spin pumping signals $V_{SP}$ can be written as [3,11]

$$V_{SP} = \left[\frac{2e}{\hbar}\theta_{SH}\lambda_{SD}\tanh\left(\frac{t_{NM}}{2\lambda_{SD}}\right)wR\right]\left[\frac{\hbar\omega}{4\pi}g_{\text{eff}}^{\uparrow\downarrow}P\sin^2\phi\right]. \quad (1)$$

The term in the first square bracket of Eq. (1) expresses the Pt-related contribution to $V_{SP}$, which influences the efficiency of spin pumping. The term in the second square bracket gives the dc spin current density ($j_s = \frac{\hbar\omega}{4\pi}g_{\text{eff}}^{\uparrow\downarrow}P\sin^2\phi$) injected into the Pt layer, $e$ is the electron charge, and $\hbar$ is the reduced Planck constant. $\theta_{SH}$ and $\lambda_{SD}$ are the spin Hall angle and spin diffusion length in the Pt layer. $R$ is the sample resistance, $w$ is the width of Pt main stripe, and $t_{NM}$ corresponds to Pt film thickness (7 nm). $\omega = 2\pi f$ is the microwave pulsation in experiments. $\phi$ is the cone angle of magnetization precession

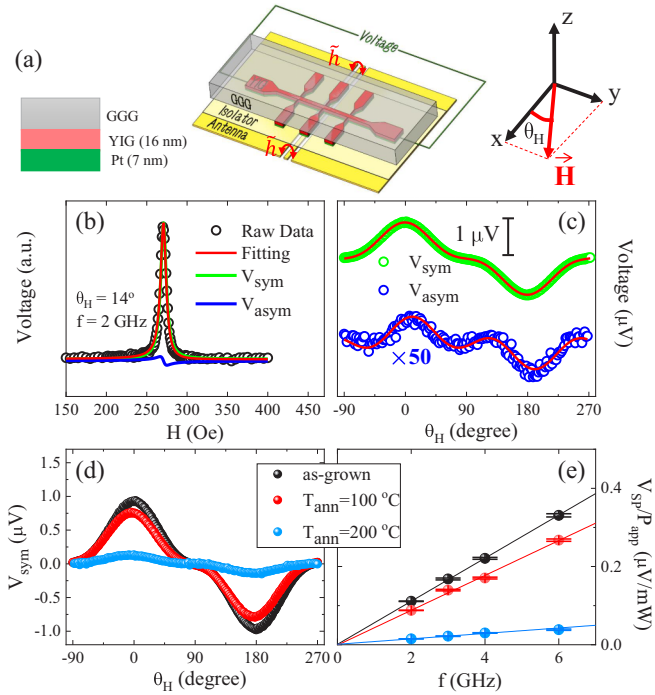


FIG. 3. Modulation of spin pumping in YIG/Pt. (a) Illustration of sample and the geometry of spin pumping measurements. (b) A representative trace of $V(H)$ data when $\theta_H$ is 14° (microwave frequency $f$ is 2 GHz and microwave power is 10 mW), plotted with the fitting by the combination of symmetric and antisymmetric Lorentzian curves. (c) Angular dependence of $V_{sym}$ and $V_{asym}$, fitted by taking SRE into consideration. $V_{asym}$ is magnified up to 50 times in order to be visualized. (d) Angular dependent $V_{sym}$ for the same sample before and after postannealing. (e) The linear dependence of $V_{SP}/P_{app}$ and frequency f. The slopes in (e) are linearly proportional to the effective spin mixing conductance.

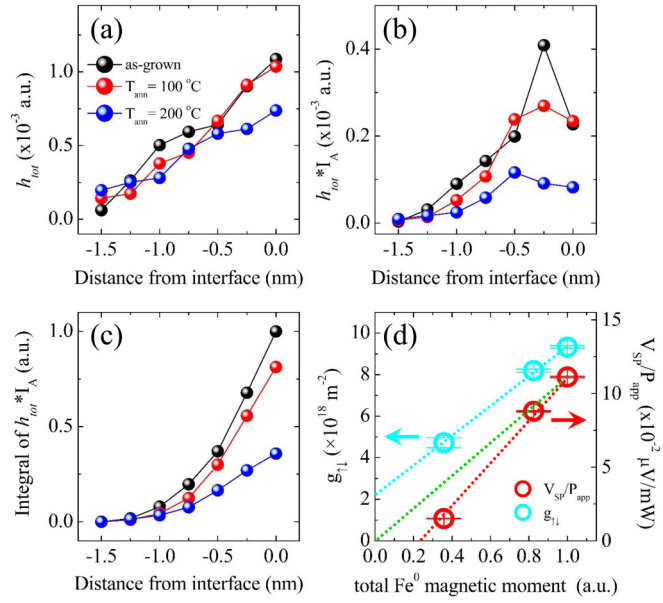


FIG. 4. Estimations of total $Fe^0$ magnetic moments in region III. (a) The calculated local $h_{tot}$, (b) the products between $h_{tot}$ and $I_A$, (c) normalized integrals of $h_{tot} * I_A$ in region III (as-grown, $T_{ann} =$ 100 °C and $T_{ann} = 200$ °C). (d) The linear dependence of $V_{SP}/P_{app}$ (red circle) and $g_{\uparrow\downarrow}$ (cyan circle) on total $Fe^0$ magnetic moments. The green dotted line illustrates the hand-waving estimation of $V_{SP}/P_{app}$ signals when considering interfacial spin loss under the situation of $\delta = 1$. The red dotted line and cyan dotted line are the guidelines to eyes.

and $P$ is the correction factor of the ellipticity of the precession. $g_{eff}^{\uparrow\downarrow}$ is the effective spin mixing conductance.

The steady Pt resistivity against annealing up to 350 °C was reported [32]. We recorded the resistances $R$ of the GGG/YIG/Pt sample before and after postannealing, which were 212.6 Ω (as grown), 204.7 Ω ($T_{ann} = 100$ °C), and 195.4 Ω ($T_{ann} = 200$ °C). The sample resistance monotonically changed by a small amount of 8% after postannealing at 200 °C. Recalling that spin Hall conductivity for Pt is dominated by intrinsic spin Hall effect from momentum-space Berry phase [33,34], Zhu *et al.* pointed out that $\theta_{SH}$ and $\lambda_{SD}$ are robust against annealing [35] and the variations of spin pumping are solely attributed to the variations of effective spin mixing conductance [36]. Thus, the Pt-related contribution to $V_{SP}$ is regarded as a robust term against postannealing, the variation of the $V_{SP}$ signal is entirely attributed to the variation of $j_s$ injected into Pt [36]. This statement is also supported by the linear dependence of $\vartheta_{SH}$ and Pt resistivity [37,38].

Spin current density $j_s$ is influenced by the precession angle $\phi$, as described by the term $P \sin^2\phi$. This term is determined by the film thickness and microwave frequency f (i.e., magnetic field H) [39,40]. As a result, it is linearly proportional to the actual microwave power applied on samples ($P_{app}$) [12]. As shown in Fig. 3(e), the normalized $V_{SP}/P_{app}$ indeed exhibit the linear dependence of frequency f, in accordance with spin pumping theory [the slopes in Fig. 3(e) correspond to $g_{eff}^{\uparrow\downarrow}$]. Therefore, we can characterize effective spin mixing conductance $g_{eff}^{\uparrow\downarrow}$ by $V_{SP}/P_{app}$ when fixing microwave frequency [41], and conclude that the dramatic reduction of $V_{SP}/P_{app}$ is attributed to the dramatic reduction of $g_{eff}^{\uparrow\downarrow}$ after postannealing at 200 °C.

The local moment model predicted that $g_{eff}^{\uparrow\downarrow}$ was not saturated when $Fe^0$ insertion layer reached four monolayers [9]. Therefore, all $Fe^0$ atoms in region III might contribute to $g_{eff}^{\uparrow\downarrow}$ and we need to estimate the total $Fe^0$ magnetic moments in region III. According to the sum rules [42], magnetic moment per Fe atom is linearly proportional to the number of holes on Fe d bands. The direct comparisons between the total numbers of holes for similar materials is permitted by the following [23]:

$$(h_{tot})_1/(h_{tot})_2 = \left[\frac{21I_{L2}}{12E_{L2}} + \frac{15I_{L3}}{12E_{L3}}\right]_1 \Big/ \left[\frac{21I_{L2}}{12E_{L2}} + \frac{15I_{L3}}{12E_{L3}}\right]_2, \quad (2)$$

where $(h_{tot})_i$ represents the total number of holes for material i, $I_{L2}$ and $I_{L3}$ are the absorption intensities of the $L_2$ edge and $L_3$ edge, $E_{L2}$ (706.6 eV) and $E_{L3}$ (705.2 eV) are the energy of $L_2$ edge and $L_3$ edge. To quantitatively characterize $Fe^0$ magnetic moments, we calculated $h_{tot} = [\frac{21I_{L2}}{12E_{L2}} + \frac{15I_{L3}}{12E_{L3}}]$ from $Fe^0$ $L$-edge spectra in region III. As shown in Fig. 4(a), the local $h_{tot}$ decreases monotonically when distancing from

YIG/Pt interface. This is consistent with the tendency of $L_3/L_2$ ratios shown in Fig. 2(b) that $Fe^0$ magnetic moments is reduced when deeply inside the Pt layer, confirming the electron transfer between Fe and Pt. Very little variations of local $h_{tot}$ were observed after postannealing except for that in $Fe^0$ enrichment zone for $T_{ann} = 200\,^{\circ}C$. Since the local $Fe^0$ atom density is characterized by $I_A$ and magnetic moment per $Fe^0$ atom is characterized by $h_{tot}$, the products between $h_{tot}$ and $I_A$ can present magnetic moment density at different locations in region III [Fig. 4(b)]. Integrating $h_{tot} * I_A$ in region III will provide the total magnetic moments of $Fe^0$ in region III. Integrals of $h_{tot} * I_A$ shown in Fig. 4(c) were normalized by the maximum value of the as-grown sample, corresponding to the normalized total $Fe^0$ magnetic moments in region III. As shown in Fig. 4(d), the linear dependence of $V_{SP}/P_{app}$ (at 2 GHz) and total $Fe^0$ magnetic moments was observed, which demonstrates the linear dependence of $g_{eff}^{\uparrow\downarrow}$ and total $Fe^0$ magnetic moments in region III. Such a linear relation was predicted by local moment model [9] and clearly evidenced in Fig. 4(d).

A noticeable discrepancy between our data in Fig. 4(d) and the prediction of local moment model is that $V_{SP}/P_{app}$ returns to zero prior to total $Fe^0$ magnetic moments. In other words, $j_s$ has been suppressed and killed when nearly a quarter of $Fe^0$ magnetic moments still exist in region III. This counterintuitive fact seems to be unreasonable unless a spin sink exists at the YIG/Pt interface. To the best of our knowledge, there are two possible mechanisms reported in the literature that might result in this spin sink at YIG/Pt interface: (1) interfacial spin loss (ISL) [41,43], (2) spin-flip process induced by MPE [44,45].

(1) ISL originates from the electron scattering at a sharp interface. ISL is characterized by a factor $\delta$. YIG/Pt interface is ideally transparent to spin current and there is no ISL when $\delta = 0$. YIG/Pt interface becomes a perfect spin sink when $\delta = 1$. Usually, $\delta$ wanders between 0.3 and 0.6 for FM/Pt system [41]. If we postulate an extreme situation when $\delta = 1$ in our samples, all spin current pumped by YIG into Pt layer would be blocked at YIG/Pt interface. Only $Fe^0$ magnetic moments in region III contribute to $j_s$ injected into Pt. Consequently, $V_{SP}/P_{app}$ signals will return to zero together with total $Fe^0$ magnetic moments [illustrated as the green dot line in Fig. 4(d)]. Obviously, our data in Fig. 4(d) cannot be accounted for by the ISL model, even under the extreme situation.

It is worth mentioning that $V_{SP}/P_{app}$ originates from spin angular momentum exchange at YIG/Pt interface. For zero $Fe^0$ magnetic moment, the magnon-electron exchange at YIG/Pt interface may produce a positive voltage signal. Thus we expect a positive $V_{SP}/P_{app}$ for zero $Fe^0$ magnetic moment when $\delta \neq 1$.

(2) A linearlike thickness dependence of the damping was revealed in FM thin films [46]. MPE induced magnetic moments in Pt will produce a similar spin-flip process [44,45], analogous to that which occurs in FM. As a result, $Fe^0$ magnetic moments in the Pt layer act as a spin sink and block spin current pumped by YIG into the Pt layer. This spin-flip process is characterized by transverse spin coherence length $\lambda_J = h v_g/2J_{ex}$, where $v_g$ is the electronic group velocity at Fermi level and $J_{ex}$ is the exchange energy of FM. Such spin-flip process would be suppressed if exchange energy $J_{ex}$ is reduced, i.e., the reduction of the total $Fe^0$ magnetic moments would suppress this spin-flip process. In consequence, the reduction of total $Fe^0$ magnetic moments would cause an increase of the $V_{SP}/P_{app}$ signal, contrary to our observations in Fig. 4(d).

Therefore, there must exist another mechanism of this spin sink effect in our sample. As we mentioned above [Fig. 2(b)], $Fe^0$ magnetic moments in the $Fe^0$ enrichment zone was dramatically reduced after postannealing at 200 °C. In contrast, $Fe^0$ atom density ($I_A$) and $Fe^0$ magnetic moment per atom ($L_3/L_2$ ratio) were barely changed in $Fe^0$ depletion zone, resulting in the robust magnetic moments in the $Fe^0$ depletion zone against postannealing. It is worth mentioning that a considerably large spin anomalous Hall effect was reported in FePt alloy [47,48]. Then it is reasonable to expect a shorter spin diffusion length $\lambda_{SD}$ in the $Fe^0$ depletion zone than that in Pt bulk [37,49], which can contribute to a channel of the spin sink effect. At present, the mechanism of this spin sink effect is an open question, a model is desired to capture the physics in such a classical system as YIG/Pt.

To verify this spin sink effect, we defined the interfacial spin mixing conductance $g_{\uparrow\downarrow}$ for YIG/PtFe interface and calculated it using Gilbert damping parameter (details described in Supplemental Material S5 [19]) [50,51]. As shown in Fig. 4(d), the linear dependence of $g_{\uparrow\downarrow}$ on total $Fe^0$ magnetic moments was revealed, which was consistent with that of $V_{SP}/P_{app}$, in support of the local moment model. However, the $g_{\uparrow\downarrow}$ value is always positive with $g_{\uparrow\downarrow}(0) = 2.4\times10^{18}\,m^{-2}$ at zero $Fe^0$ magnetic moment, inconsistent with $V_{SP}/P_{app}$. This $g_{\uparrow\downarrow}(0)$ might represent the true spin pumping at YIG/Pt interface without the $Fe^0$ magnetic moment. Recall that $g_{\uparrow\downarrow}$ is equivalent to the spin current out of the YIG layer. On the other hand, $V_{SP}/P_{app}$ (corresponds to $g_{eff}^{\uparrow\downarrow}$) characterizes the efficiency of spin injection from YIG into Pt bulk. In the presence of the interfacial spin sink effect, the spin current out of the YIG should always be greater than the spin current injected into Pt bulk ($g_{\uparrow\downarrow} > g_{eff}^{\uparrow\downarrow}$) with their difference being the spin loss in the interfacial region. Therefore, the discrepancy between $g_{\uparrow\downarrow}$ and $V_{SP}/P_{app}$ confirmed the existence of the spin sink effect at the YIG/Pt interface unambiguously. It is worth mentioning that interfacial spin sink effect has the same YIG-thickness scaling as $g_{\uparrow\downarrow}$, making it very challenging to isolate the spin sink effect from $g_{\uparrow\downarrow}$ [36]. In addition, the oxygen deficiency and the existence of $Fe^{2+}$ cations due to the deposition of Pt layer will also induce an additional Gilbert damping, leading to the unphysical estimation of $g_{\uparrow\downarrow}$ [3]. Therefore, $V_{SP}/P_{app}$ is a good parameter to describe the spin injection efficiency of the entire YIG/Pt interfacial region, in contrast to $g_{\uparrow\downarrow}$.

As we defined $g_{\uparrow\downarrow}$ for the sharp YIG/PtFe interface, defining the interfacial spin mixing conductance $g_{PtFe/Pt}^{\uparrow\downarrow}$ for the interface between the PtFe and Pt layer is not appropriate because PtFe in region III is spatially nonuniform. In order to achieve a more precise description of such spatially nonuniform system, a different theoretical model should be introduced in the future.

Overall, the existence of $Fe^0$ magnetic moments at YIG/Pt interface can enhance spin pumping (like a "spin current amplifier"), meanwhile PtFe alloying may contribute to a new channel of spin sink. The competition between these two effects will result in the actual spin pumping across the YIG/Pt interface. Supposing we modified YIG/Pt interface by inserting an $Fe^0$ atom, a large amount of $Fe^0$ atom insertion (e.g. one atomic layer of $Fe^0$) would significantly enhance $g_{\text{eff}}^{\uparrow\downarrow}$, analogous to our case of as-grown sample. On the contrary, a small amount of $Fe^0$ atoms would diminish $g_{\text{eff}}^{\uparrow\downarrow}$, similar to our case of $T_{\text{ann}} = 200\,^{\circ}\text{C}$. Then the contradictory experimental results [10,11] may also be explained according to our observations in Fig. 4(d). It is worth mentioning that SMR decreases by 61% after annealing [52], which might be relevant to our observations.

In summary, a sharp structural interface between YIG and Pt in the GGG/YIG/Pt sample was revealed by atomically resolved EELS and STEM. $Fe^0$ diffusion into Pt layer was confirmed unambiguously. Tailoring the YIG/Pt interface by postannealing, the linear dependence of $g_{\text{eff}}^{\uparrow\downarrow}$ and total $Fe^0$ magnetic moments was demonstrated, revealing the critical role of the interfacial magnetic moments on spin mixing conductance. Furthermore, $V_{SP}/P_{\text{app}}$ was found return to zero previous to the total $Fe^0$ magnetic moments, indicating a different channel of spin sink at the YIG/Pt interface. Such a spin sink effect may be attributed to the curtailed spin diffusion length in PtFe.

This work was financially supported by the National Key Research and Development Program of China (Grants No. 2016YFA0300804 and No. 2017YFA0303303), National Natural Science Foundation of China (Grants No. 11874072, No. 51672007, No. 11974023, and No. 11674159), Key-Area Research and Development Program of GuangDong (Grants No. 2018B030327001 and No. 2018B010109009), and the "2011 Program" Peking-Tsinghua-IOP Collaborative Innovation Center for Quantum Matter. X.R.W. is supported by Hong Kong RGC (Grants No. 16301518 and No. 16301619).

[1] F. Hellman, A. Hoffmann, Y. Tserkovnyak *et al.*, Rev. Mod. Phys. **89**, 025006 (2017).
[2] A. V. Chumak, V. I. Vasyuchka, A. A. Serga, and B. Hillebrands, Nat. Phys. **11**, 453 (2015).
[3] F. Yang and P. Chris Hammel, J. Phys. D **51**, 253001 (2018).
[4] B. Heinrich, C. Burrowes, E. Montoya, B. Kardasz, E. Girt, Y.-Y. Song, Y. Sun, and M. Wu, Phys. Rev. Lett. **107**, 066604 (2011).
[5] D. Meier, D. Reinhardt, M. van Straaten *et al.*, Nat. Commun. **6**, 8211 (2015).
[6] C. O. Avci, A. Quindeau, C.-F. Pai, M. Mann, L. Caretta, A. S. Tang, M. C. Onbasli, C. A. Ross, and G. S. D. Beach, Nat. Mater. **16**, 309 (2017).
[7] H. Nakayama, M. Althammer, Y.-T. Chen *et al.*, Phys. Rev. Lett. **110**, 206601 (2013).
[8] Y. Tserkovnyak, A. Brataas, and E. W. Bauer, Phys. Rev. Lett. **88**, 117601 (2002).
[9] X. Jia, K. Liu, K. Xia, and E. W. Bauer, Europhys. Lett. **96**, 17005 (2011).
[10] C. Burrowes, B. Heinrich, B. Kardasz, E. A. Montoya, E. Girt, Y. Sun, Y.-Y. Song, and M. Wu, Appl. Phys. Lett. **100**, 092403 (2012).
[11] S. Emori, A. Matyushov, H.-M. Jeon *et al.*, Appl. Phys. Lett. **112**, 182406 (2018).
[12] M. B. Jungfleisch, V. Lauer, R. Neb, A. V. Chumak, and B. Hillebrands, Appl. Phys. Lett. **103**, 022411 (2013).
[13] Z. Qiu, K. Ando, K. Uchida, Y. Kajiwara, R. Takahashi, H. Nakayama, T. An, Y. Fujikawa, and E. Saitoh, Appl. Phys. Lett. **103**, 092404 (2013).
[14] S. Pütter, S. Geprägs, R. Schlitz, M. Althammer, A. Erb, R. Gross, and S. T. B. Goennenwein, Appl. Phys. Lett. **110**, 012403 (2017).
[15] H. Babu Vasili, M. Gamino, J. Gàzquez, F. Sánchez, M. Valvidares, P. Gargiani, E. Pellegrin, and J. Fontcuberta, ACS Appl. Mater. Interfaces **10**, 12031 (2018).
[16] Y. Kang, H. Zhong, R. Hao *et al.*, Chinese Phys. B **26**, 047202 (2017).
[17] M. Liu, L. Jin, J. Zhang, Q. Yang, H. Zhang, P. Gao, and D. Yu, AIP Adv. **8**, 085117 (2018).
[18] C. Colliex, T. Manoubi, and C. Ortiz, Phys. Rev. B **44**, 11402 (1991).
[19] See Supplemental Material at http://link.aps.org/supplemental/10.1103/PhysRevB.102.014411 for further details of sample fabrication and of STEM and EELS experiments, spin pumping experiment, the cross-sectional composition maps of sample, the analysis of EELS spectrum, the discussion of magnetic proximity effect at YIG/Pt interface.
[20] P. Wang, H. Zhao, S. Liu *et al.*, Appl. Phys. Lett. **113**, 182402 (2018).
[21] Y. Y. Chin, H.-J. Lin, Y.-F. Liao *et al.*, Phys. Rev. B **99**, 184407 (2019).
[22] D. J. Huang, C. F. Chang, H.-T. Jeng *et al.*, Phys. Rev. Lett. **93**, 077204 (2004).
[23] T. I. Morrison, M. B. Brodsky, N. J. Zaluzec, and L. R. Sill, Phys. Rev. B **32**, 3107 (1985).
[24] S. Kim, K. Ueda, G. Go *et al.*, Nat. Commun. **9**, 1648 (2018).
[25] X. Liang, Y. Zhu, B. Peng, L. Deng, J. Xie, H. Lu, M. Wu, and L. Bi, ACS Appl. Mater. Interfaces **8**, 8175 (2016).
[26] K. He, Y. Zhou, P. Gao *et al.*, ACS Nano **8**, 7251 (2014).
[27] M. Harder, Y. Gui, and C.-M. Hu, Phys. Rep. **661**, 1 (2016).
[28] M. B. Jungfleisch, W. Zhang, J. Sklenar *et al.*, Phys. Rev. Lett. **116**, 057601 (2016).
[29] P. Wang, S. W. Jiang, Z. Z. Luan, L. F. Zhou, H. F. Ding, Y. Zhou, X. D. Tao, and D. Wu, Appl. Phys. Lett. **109**, 112406 (2016).
[30] S. Keller, J. Greser, M. R. Schweizer, A. Conca, V. Lauer, C. Dubs, B. Hillebrands, and E. Th. Papaioannou, Phys. Rev. B **96**, 024437 (2017).
[31] R. Iguchi and E. Saitoh, J. Phys. Soc. Jpn. **86**, 011003 (2017).
[32] C. O. Avci, A. Quindeau, M. Mann, C.-F. Pai, C. A. Ross, and S. D. Beach, Phys. Rev. B **95**, 115428 (2017).

[33] G. Y. Guo, S. Murakami, T.-W. Chen, and N. Nagaosa, Phys. Rev. Lett. **100**, 096401 (2008).
[34] L. J. Zhu, D. C. Ralph, and R. A. Buhrman, Phys. Rev. Appl. **10**, 031001 (2018).
[35] L. J. Zhu, D. C. Ralph, and R. A. Buhrman, Phys. Rev. B **98**, 134406 (2018).
[36] L. Zhu, D. C. Ralph, and R. A. Buhrman, Phys. Rev. Lett. **123**, 057203 (2019).
[37] L. Wang, R. J. H. Wesselink, Y. Liu, Z. Yuan, K. Xia, and P. J. Kelly, Phys. Rev. Lett. **116**, 196602 (2016).
[38] E. Sagasta, Y. Omori, M. Isasa, M. Gradhand, L. E. Hueso, Y. Niimi, Y. Otani, and F. Casanova, Phys. Rev. B **94**, 060412(R) (2016).
[39] K. Ando, T. Yoshino, and E. Saitoh, Appl. Phys. Lett. **94**, 152509 (2009).
[40] O. Mosendz, V. Vlaminck, J. E. Pearson, F. Y. Fradin, G. E. W. Bauer, S. D. Bader, and A. Hoffmann, Phys. Rev. B **82**, 214403 (2010).
[41] X. Tao, Q. Liu, B. Miao *et al.*, Sci. Adv. **4**, eaat1670 (2018).
[42] C. T. Chen, Y. U. Idzerda, H.-J. Lin, N. V. Smith, G. Meigs, E. Chaban, G. H. Ho, E. Pellegrin, and F. Sette, Phys. Rev. Lett. **75**, 152 (1995).
[43] K. Chen and S. Zhang, Phys. Rev. Lett. **114**, 126602 (2015).
[44] M. Caminale, A. Ghosh, S. Auffret, U. Ebels, K. Ollefs, F. Wilhelm, A. Rogalev, and W. E. Bailey, Phys. Rev. B **94**, 014414 (2016).
[45] T. A. Peterson, A. P. McFadden, C. J. Palmstrøm, P. A. Crowell, N. V. Smith, G. Meigs, E. Chaban, G. H. Ho, E. Pellegrin, and F. Sette, Phys. Rev. B **97**, 020403(R) (2018).
[46] A. Ghosh, S. Auffret, U. Ebels, and W. E. Bailey, Phys. Rev. Lett. **109**, 127202 (2012).
[47] K. M. Seemann, Y. Mokrousov, A. Aziz *et al.*, Phys. Rev. Lett. **104**, 076402 (2010).
[48] T. Seki, S. Iihama, T. Taniguchi, and K. Takanashi, Phys. Rev. B **100**, 144427 (2019).
[49] Y. Ou, D. C. Ralph, and R. A. Buhrman, Phys. Rev. Lett. **120**, 097203 (2018).
[50] H. Wang, C. Du, P. Chris Hammel, and F. Yang, Appl. Phys. Lett. **110**, 062402 (2017).
[51] L. Wang, Z. Lu, J. Xue, P. Shi, Y. Tian, Y. Chen, S. Yan, L. Bai, and M. Harder, Phys. Rev. Appl. **11**, 044060 (2019).
[52] H. Bai, X. Z. Zhan, G. Li, J. Su, Z. Z. Zhu, Y. Zhang, T. Zhu, and J. W. Cai, Appl. Phys. Lett. **115**, 182401 (2019).